Extraction of Moho-Generated Phases from Vertical and Radial Receiver Functions of a Seismic Array

by Takashi Tonegawa,[*] Ryohei Iritani, and Hitoshi Kawakatsu

Abstract   Receiver-function analysis is an effective tool for investigating crustal seismological structure. Here, we present the extraction of the Moho-reflected $PpPp$ that emerges in teleseismic P coda via a deconvolution process. Using nonlinear waveform analysis (an approach using simulated annealing technique) we estimate the source wavelet of a teleseismic P wave from records of the vertical component observed at an array of seismometers. $PpPp$ recorded on the vertical component can be extracted by deconvolving individual vertical components by the resulting source wavelet. By employing this technique in a case study in southwestern Japan, seismic images from $PpPp$, as well as from Ps and $PpPs$, successfully image the continental Moho, the oceanic Moho, and the top surface of the Philippine Sea slab. In addition, we found that the amplitude of $PpPp$ is useful in precisely determining crustal properties, such as vertically averaged V_P/V_S and the crustal thickness, by grid-search techniques. It is also important to take into account the variations of the conversion/reflection coefficients for decreasing errors of the parameters in the grid-search technique. Moreover, we demonstrate that improved seismic images of horizontal discontinuities can be obtained by using a stacking technique.

Introduction

Seismic velocity discontinuities are present at various depths in the Earth's interior. The detection of seismic phases that are converted or reflected at such discontinuities is useful in investigating the Earth's layered structure. The receiver function (RF) technique (Langston, 1977, 1979; Owens *et al.*, 1984; Ammon, 1991) is effective in extracting P-to-S converted phases (Ps phase in Fig. 1) generated at such discontinuities. It has been used to detect various kinds of seismic velocity boundaries, including the Moho (e.g., Kind *et al.*, 1995; Sheehan *et al.*, 1995), upper mantle discontinuities (e.g., Li *et al.*, 2000), and dipping layers associated with subducting slabs (e.g., Yuan *et al.*, 2000; Ferris *et al.*, 2003).

Assuming a vertically averaged crustal P-wave velocity V_P, previous studies have also used RFs to determine the crustal seismic structure, namely, the crustal thickness and the vertically averaged crustal V_P/V_S, for which V_S is the vertically averaged crustal S-wave velocity (e.g., Zandt *et al.*, 1995; Chevrot and van der Hilst, 2000; Zhu and Kanamori, 2000). These estimations were performed using grid-search techniques; the one introduced by Zhu and Kanamori (2000) is commonly used with the amplitude of converted and/or reflected phases, including Ps, $PpPs$, and $PpSs$, in the radial component of the RFs. However, because a suite of RF

traces used in the stacking technique has a wide range of signal-to-noise ratios (SNR), there is sometimes a large error in the resulting estimation of crustal thickness and V_P/V_S. To increase SNR in the stacking technique when estimating those values, it would be useful if other phases, such as $PpPp$ in the vertical component of the RF, could be simultaneously employed. Moreover, as will be discussed later, the use of the $PpPp$ could contribute to improving the accuracy of the stacking techniques.

In this study, we attempt to isolate $PpPp$ phases in the teleseismic P coda, and apply them to a grid-search technique that uses Ps, $PpPs$, and/or $PpSs$ in the radial component (Fig. 1). Ps and $PpPs$ phases can be extracted by calculating conventional RFs, whereas the incoming wavelet of teleseismic P waves must be estimated in order to isolate $PpPp$ in the vertical component; we refer to these receiver functions as radial and vertical RFs, respectively. The incoming wavelet contains not only the source–time function but also surface-reflected phases around the source region. Nevertheless, we refer to it as a source wavelet in this paper to indicate an incoming teleseismic wavelet to the array. In previous studies, using records from an array of seismometers, the source wavelet has been estimated by using three different approaches: singular value decomposition (SVD; Bostock and Rondenay, 1999; Bostock *et al.*, 2001; Rondenay *et al.*, 2001; Shragge *et al.*, 2001), waveform-stacking techniques (Li and Nábělek,

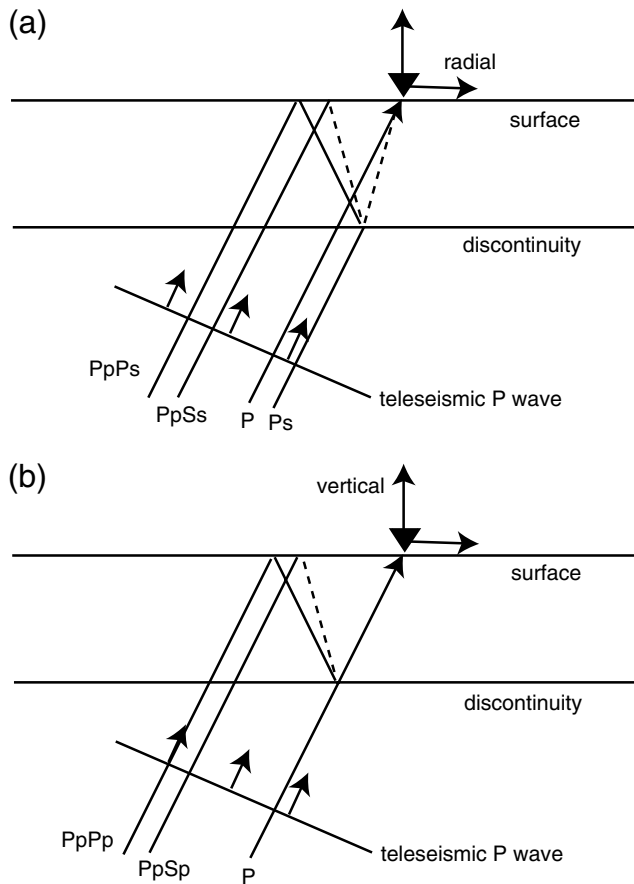*Also at Earthquake Research Institute, The University of Tokyo, 1-1-1 Yayoi, Bunkyo-ku, Tokyo 113-0032.

(a)

radial

surface

discontinuity

PpPs

PpSs P Ps

teleseismic P wave

(b)

vertical

surface

discontinuity

PpPp

PpSp P

teleseismic P wave

Figure 1. Ray paths of the Ps-converted phase recorded on the radial component, $PpPs$ reflected at a discontinuity and recorded on the radial component, and $PpPp$ reflected at a discontinuity and recorded on the vertical component, all isolated from a teleseismic P wave.

400 km

Japan Trench

A′ KACH

Sagami Trough

Chugoku

36° N

Shikoku

34° N

100 km SSKH A

Nankai trough

32° N

130° E 132° E 134° E 136° E 138° E

Figure 2. Locations of Hi-net stations employed in this study and the location of line AA′.

Vertical RFs Deconvolved by Source Wavelets that are Estimated with Different Approaches section.

In subsequent sections, we explain the tectonic setting including the undulation of the Moho in southwestern Japan, which is important for discussing estimation of the source wavelet. We show how the undulation of the Moho is necessary to successfully estimate source wavelets by employing numerical simulations. Moreover, we introduce seismic images and stacking techniques using $PpPp$, and explain why $PpPp$ is useful for estimating crustal properties.

Tectonic Setting of Southwestern Japan

In southwestern Japan, the Philippine Sea slab is subducting to the west-northwest at the Nankai Trough (Fig. 2) at a subduction velocity of 6–7 cm/yr (Miyazaki and Heki, 2001). The configuration of the top surface of the Philippine Sea slab and the oceanic Moho within the slab has been investigated using several seismological approaches, including P- and S-wave tomography (Nakajima and Hasegawa, 2007; Hirose *et al.*, 2008) and RF (Yamauchi *et al.*, 2003; Shiomi *et al.*, 2004, 2006; Ramesh *et al.*, 2005; Ueno *et al.*, 2008a,b). In particular, Shiomi *et al.* (2006) determined the geometry of the oceanic Moho at depths of 25–60 km and of the continental Moho at depths of 25–40 km. Katsumata (2010) estimated the configuration of the continental Moho beneath the Japanese islands by using travel-time analysis of P and S waves, and obtained results that were consistent with those of Shiomi *et al.* (2004) for southwestern Japan.

Seismic velocity models that include the crust and uppermost mantle have also been determined from seismic-exploration surveys (e.g., Ito *et al.*, 2009), P- and S-wave tomography (e.g., Matsubara *et al.*, 2008), travel-time analysis of body waves (Katsumata, 2010), hypocenter distributions (Miyoshi and Ishibashi, 2004), and the free-surface-reflected sP phase (Hayashida *et al.*, 2010). Interestingly, although the seismological structure in southwestern Japan

1999; Langston and Hammer, 2001), and the nonlinear waveform analysis (e.g., Chevrot, 2002; Garcia *et al.*, 2004; Iritani *et al.*, 2010) which is used in this work. We employ a nonlinear waveform analysis based on simulated annealing (SA; e.g., Sen and Stoffa, 1995) to obtain the source wavelet of the teleseismic P wave observed at seismometers located in southwestern Japan, and we remove the source wavelet from each trace via deconvolution. This technique is employed because information on the relative arrival time can be obtained simultaneously with the source wavelet. By minimizing the appropriate cost function, the obtained source wavelet would be plausible compared with that estimated by the linear stacking technique. SVD is useful for extracting coherent phases from a large number of seismograms. The advantages of SA over SVD may not be obvious, but there seems to be an ambiguity in choosing the number of principal components to represent the source wavelet of each teleseismic event in SVD. In addition, it seems that our result shows an advantage of SA relative to both SVD and linear stacking under the conditions found in this study, including the number of stations and the degree of Moho undulation, as will be discussed in the
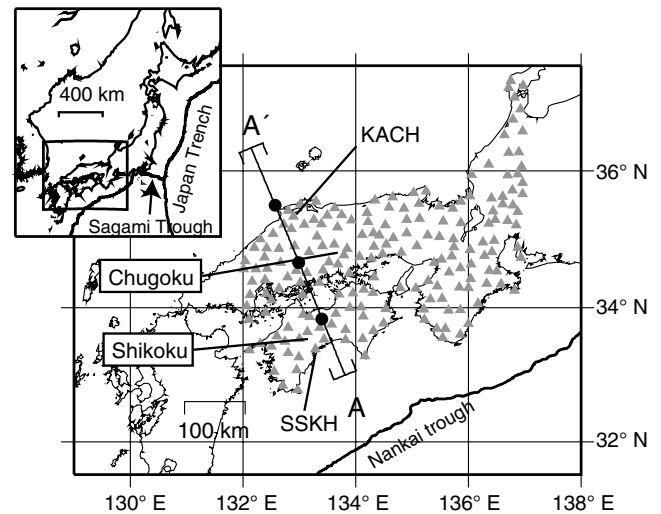
has been assessed in these studies, Ide *et al.* (2010) were the first to report that a split along the subducted extinct ridge within the Philippine Sea slab is inducing an abrupt change in depth of the slab, by up to approximately 50 km. In contrast to the significant structural change in the uppermost mantle, tomographic studies show small perturbations in seismic velocity within the crust beneath southwestern Japan (e.g., Nishida *et al.*, 2008). In summary, based on these seismological observations, it is apparent that the seismic boundaries associated with the Philippine Sea slab beneath southwestern Japan, including the oceanic Moho and the top surface of the slab, are strongly undulating (25–60 km for the oceanic Moho), whereas the continental Moho is relatively strongly undulating (25–40 km), and the crust is characterized by a weakly heterogeneous structure. These crustal properties (i.e., the relatively strong undulation of the Moho and weak crustal heterogeneities) enable us to effectively retrieve the source wavelet by SA.

Data

We examine seismograms of earthquakes that occurred from February 2001 to August 2010 at epicentral distances between 30° and 90°, and with $5.5 \leq M \leq 6.9$. From a total of 600 events, we chose ~300 events with an impulsive *P* wave. When applying SA to seismograms, we found that the first arrival of the direct *P* wave should have larger amplitude than later arrivals, such as the depth phases of deep and intermediate-depth earthquakes. This is because the estimation of the source wavelet with SA is strongly dependent on the amplitude of the seismic phase. If the amplitude of the direct *P* wave is smaller than those of later arrivals, the estimations of both the source wavelet and the time shifts would be of the phase with the largest amplitude among the later arrivals. Therefore, in this study, we avoided using events for which the amplitude of the direct *P* wave is smaller than or comparable to that of later phases.

The teleseismic events were recorded on short-period (1 Hz) sensors of Hi-net (station spacing of ~20 km), which is operated by the National Research Institute for Earth Science and Disaster Prevention (NIED), Japan (Okada *et al.*, 2004). At each station, three components of ground velocity are measured at a sampling rate of 100 Hz. We removed the instrument response from the raw data by deconvolution, and resampled the data at 20 Hz. We employed stations located between 132° E and 137° E in longitude (Fig. 2). The amplitudes of teleseismic *P* coda on the radial and vertical components are normalized by the maximum amplitude of the direct *P* wave in the vertical component.

Methods for Retrieving Phases from the Vertical RF

Nonlinear Waveform Analysis for the Teleseismic *P*-Source Wavelet Using SA

Chevrot (2002) demonstrated that the source wavelet of the teleseismic *P* wave and its relative arrival time could be

estimated using SA. The SA optimization algorithm is based on a Monte Carlo technique for finding an optimal solution, which minimizes a cost function defined by an unknown model waveform and observed waveforms. Although the term model waveform is used in the same sense as source wavelet in this study, we use the term model waveform for explaining the processing of SA in this section, following previous papers related to SA.

Seismic records of teleseismic *P* waves can be modeled as follows:

$$S_i(t) = W(t - \tau_i), \tag{1}$$

where $S_i(t)$ is the model waveform at the *i*th station, $W(t)$ is the reference waveform of the teleseismic *P* wave, and τ_i is the time shift of the *P* wave with respect to the beginning of the record at the *i*th station. By normalizing the amplitude observed in the vertical component by its maximum amplitude, we avoided having to make amplitude a parameter. An optimal estimate of the source wavelet and its time shifts is obtained by minimizing the L1 norm misfit as follows:

$$E = \sum_i \int |D_i(t) - S_i(t)| dt, \tag{2}$$

where $D_i(t)$ is the observed waveform at the *i*th station. Minimizing the cost function E, estimated by the summation over *i* in equation (2), the model waveform, which represents the source wavelet and excludes $PpPp$, could be retrieved because the $PpPp$ does not appear coherently due to crustal thickness variation. The processing followed the algorithm described by Chevrot (2002) and its modified versions (Garcia *et al.*, 2004; Iritani *et al.*, 2010).

At each iteration step, we first perturb $W(t)$ and then determine τ_i by time shifting the previously estimated $W(t)$. The perturbation is accepted only when the misfit function decreases with the estimation of $W(t)$, whereas the acceptance of the perturbation related to time shifts depends on the probability defined by Chevrot (2002). The time window is set as −5 to 45 s from the theoretical arrival time of the *P* wave (Fig. 3a). The theoretical arrival time is calculated using the IASP91 velocity model (Kennett and Engdahl, 1991) and the frequency band is 0.07–0.7 Hz. The other parameters related to SA are the same as those used in Iritani *et al.* (2010). The total number of iterations is approximately 2000. Figure 3a,b shows examples of model waveforms and observed waveforms, respectively. In addition, Figure 3a shows that the direct *P* waves have larger amplitude than the later arrivals, as discussed in the previous section.

Construction of Radial and Vertical RFs

Because the source wavelet estimated by SA does not contain $PpPp$, which is confirmed by numerical simulations in the Synthetic Test for Estimation of Source Wavelets by SA section, $PpPp$ in the vertical component can be extracted by deconvolution with the source wavelet. In turn, $PpPp$ in
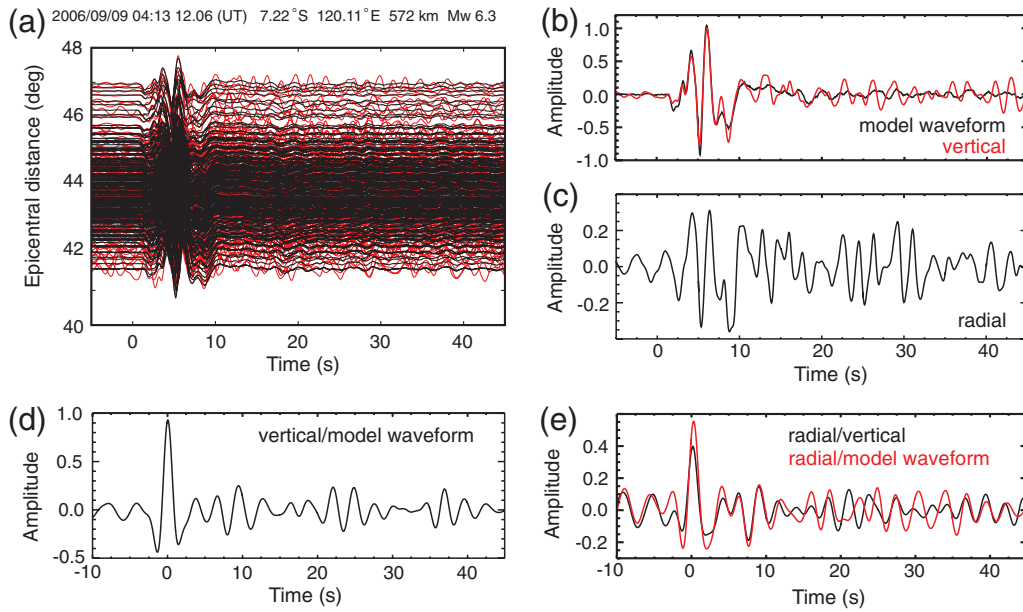
Figure 3. Examples of raw waveform data, model waveform estimated using SA, and radial and vertical RFs for an event at 04:13 (UT) on 9 September 2006 (7.22° S, 120.11° E; 572.0-km depth; M_w 6.3). (a) Black and red lines represent the model waveform, $S_i(t)$, and the observed waveform, $D_i(t)$, respectively, aligned as a function of epicentral distance; (b) black and red lines represent the model waveform and the observed waveform, respectively, for the vertical component of station NMKH (see Fig. 2 for station location); (c) observed waveform for the radial component of station NMKH; (d) example waveform of a vertical RF calculated using the waveforms shown in (b); (e) black line indicates the radial component (c) vertical component (b), whereas the red line indicates the radial component (c) model waveform (b).

the radial component, which generally has low amplitude, should be preserved in the radial RF deconvolved by the source wavelet. Such a radial RF would be useful when calculating P-wave vector RF by a linear transformation removing the free-surface response (Reading *et al.*, 2003). However, in this study, we only focus on the phase from the vertical component. The radial RF is therefore constructed in the conventional manner (i.e., deconvolved by the vertical component), whereas the vertical component is deconvolved by the source wavelet estimated by SA to extract $PpPp$ (Fig. 3b,d). Here, the source wavelet is time shifted by time τ_i, *as* estimated by SA. For comparison, Figure 3e shows radial RFs deconvolved by the vertical component (black line) and by the source wavelet (red line), indicating that the two functions are similar from −10 to 15 s, but dissimilar from 15 to 35 s. This result arises because the radial RF obtained using the source wavelet is contaminated by $PpPp$ reflected at dipping discontinuities (e.g., the Philippine Sea slab) in the uppermost mantle.

The deconvolution is conducted in the frequency domain via spectral division, and the water level for deconvolution is set to 0.01. The frequency bands are 0.2–1.0 Hz for Ps, and 0.1–0.5 Hz for $PpPp$ and $PpPs$. These values are chosen because, at Moho depths, all of these phases within these frequency bands are effectively produced by seismic discontinuities with thicknesses of less than ∼5 km (1/2-P wavelength for the Ps converted phase (Bostock, 1999), and 1/4-P wavelength for the $PpPp$ and $PpPs$ reflected phases

(Wilson and Aster, 2005). Although the Hi-net consists of short-period sensors, a seismogram of teleseismic P coda with frequencies higher than 0.1 Hz becomes available after applying correction for instrument response. RF images with a frequency band of 0.1–0.5 Hz have successfully displayed the bottom of the serpentine layer above the subducting Pacific slab (Kawakatsu and Watada, 2007), as well as a metastable wedge within the subducting Pacific slab (Kawakatsu and Yoshioka, 2011).

We assume that seismograms of the incoming teleseismic P wave are very similar throughout the array of seismometers. Although the size of the array is small (Fig. 2), we sometimes observe P arrivals with small/zero amplitude, owing to source mechanism. In this case, the SA algorithm will not accurately determine the source wavelet. To avoid this complication, we manually remove all events with small/zero P amplitudes before applying SA. The similarity between the source wavelet and vertical component seismograms can be evaluated from the amplitude of the vertical RF at 0 s time lag. We discard all RF traces for which the amplitude of the vertical RF at 0 s time lag falls outside the range 0.6–1.4. The number of source–receiver pairs employed is ∼35,000.

Synthetic Test for Estimation of Source Wavelets by SA

The use of SA to estimate the source wavelet requires relatively large lateral variations in the depth of seismic

discontinuities beneath each station within the array, in addition to the assumption that the source wavelet of the teleseismic *P* wave is the same over the entire array. For example, if the crustal thickness is uniform over the array, the waveform estimated by SA will contain $PpPp$ reflected at the Moho. Hence, the appearance of $PpPp$ reflected at the Moho in individual traces will be removed through deconvolution using the waveform. However, if the depths of the Moho and other discontinuities vary significantly over the array, the arrival times of $PpPp$ are also perturbed. As a result, the waveform estimated by SA represents only the source wavelet of the teleseismic *P* wave, indicating that $PpPp$ reflected at the discontinuities can be extracted successfully. Beneath southwestern Japan, several seismological studies have reported significant depth variations in the continental Moho and seismic discontinuities related to the Philippine Sea slab (e.g., Shiomi *et al.*, 2006; Katsumata, 2010). These observations support the proposal that the waveform estimated by SA represents a plausible source wavelet of the teleseismic *P* wave. In the section below, we briefly test whether the degree of the undulation of the Moho is sufficient to successfully estimate the source wavelet by employing numerical simulations.

Lateral Variations in the Crust

It is necessary to confirm that lateral variations in the structure of the crust in southwestern Japan are sufficiently large to suppress $PpPp$ and allow the use of SA to estimate a source wavelet. The travel time of $PpPp$ reflected at the Moho is affected by lateral variations in both crustal thickness and V_P. In this region, the crustal thickness varies from 25 to 40 km (Shiomi *et al.*, 2006), and the absolute value of the *P*- and *S*-wave velocity perturbations at crustal depths is 10% at most (Hirose *et al.*, 2008). We roughly estimate the effect with respect to the travel time of $PpPp$ by calculating the one-way travel time of vertical *P*-wave propagation between the ground surface and the Moho. Assuming $V_P = 6.35$ km/s and a crustal thickness of 25 km, a change in crustal thickness from 25- to 40-km depth results in $(40/6.35) - (25/6.35) = 2.36$ s, and a 10% reduction in V_P down to 25-km depth results in $25/(6.35 \times 0.9) - (25/6.35) = -0.44$ s. The variation in crustal thickness affects the travel time of $PpPp$ more than that of V_P. We therefore test the effect of lateral variations in the crust by only changing crustal thickness.

Synthetic Waveforms for Three Models of Crustal Thickness

We computed synthetic waveforms for the following three models: (1) crustal thickness from RF images using *Ps* converted phases, as will be discussed in the Seismic Images Using the Three Phases section; (2) crustal thickness randomly varied between 18- and 38-km depth using a random number generator; and (3) crustal thickness varied with

a Gaussian distribution within ± 10 km from 28-km depth, determined using a Gaussian random number generator (Box and Muller, 1958). We refer to these models as Observational model, Random model, and Gaussian model, respectively. A crustal thickness is assigned to the location of each Hi-net station. We used $V_P = 6.35$ km/s and $V_S = 3.65$ km/s in the crust, and the mantle-velocity structure of the IASP91 velocity model (Kennett and Engdahl, 1991) at depths greater than the Moho. The synthetic waveform was calculated by applying the generalized ray theory (Langston, 1977) to the 1D horizontal layered structure defined at each station. The frequency band is 0.07–0.7 Hz. The slowness range from the event location (10.0° S, 170.0° E, 30-km depth) to the locations of the Hi-net stations used is from 0.0636 to 0.0653 s/km.

Figure 4 shows synthetic waveforms for the three models aligned as a function of the crustal thickness. The *P*-wave first arrivals of the individual seismograms are aligned to 5 s. The synthetic waveforms for the three models show that two later phases with large amplitudes can be seen within a time window of 10–25 s (Fig. 4g–i). Because we calculated the wave field only at the receiver side, these phases are generated at the Moho. Based on the travel times of these phases, the earlier arrival corresponds to $PpPp$, whereas the candidates for the later arrival are considered to be $PsPp$, $PpPs$, and $PpSp$. Among these phases, the amplitudes of the first two phases on the vertical component are significantly smaller than that of $PpSp$, indicating that the amplitude of the later arrival is mainly due to $PpSp$. The amplitude of $PpPp$ is significantly larger than that of $PpSp$ at near vertical incidence (slowness of ~0.05 s/km), but at slownesses close to 0.08 s/km, the amplitudes of both phases become comparable. This means that seismic images generated using $PpPp$ at upper mantle depths may be obscured by the amplitude of $PpSp$. To avoid this contamination in seismic images, it may be desirable to reduce the contribution of $PpPp$ to the seismic image when making seismic images with many stacked phases, or to limit the slowness range of the events used according to the predicted amplitude of $PpSp$ when making the seismic image of $PpPp$. Alternatively, including the amplitude of $PpSp$ in the summation of seismic images could also be an effective way to improve upper mantle imaging.

Vertical RFs Deconvolved by Source Wavelets that are Estimated with Different Approaches

We applied SA to the synthetic waveforms shown in Figure 4g–i, with the same conditions as those in the Nonlinear Waveform Analysis for the Teleseismic *P* Source Wavelet Using SA section. Figure 5a–c shows the source wavelets obtained for the Observational model, Random model, and Gaussian model, respectively. The waveforms in Figure 5a,b shows the successful suppression of later phases reflected at the Moho, indicating that the waveform obtained represents a good source wavelet. However, the
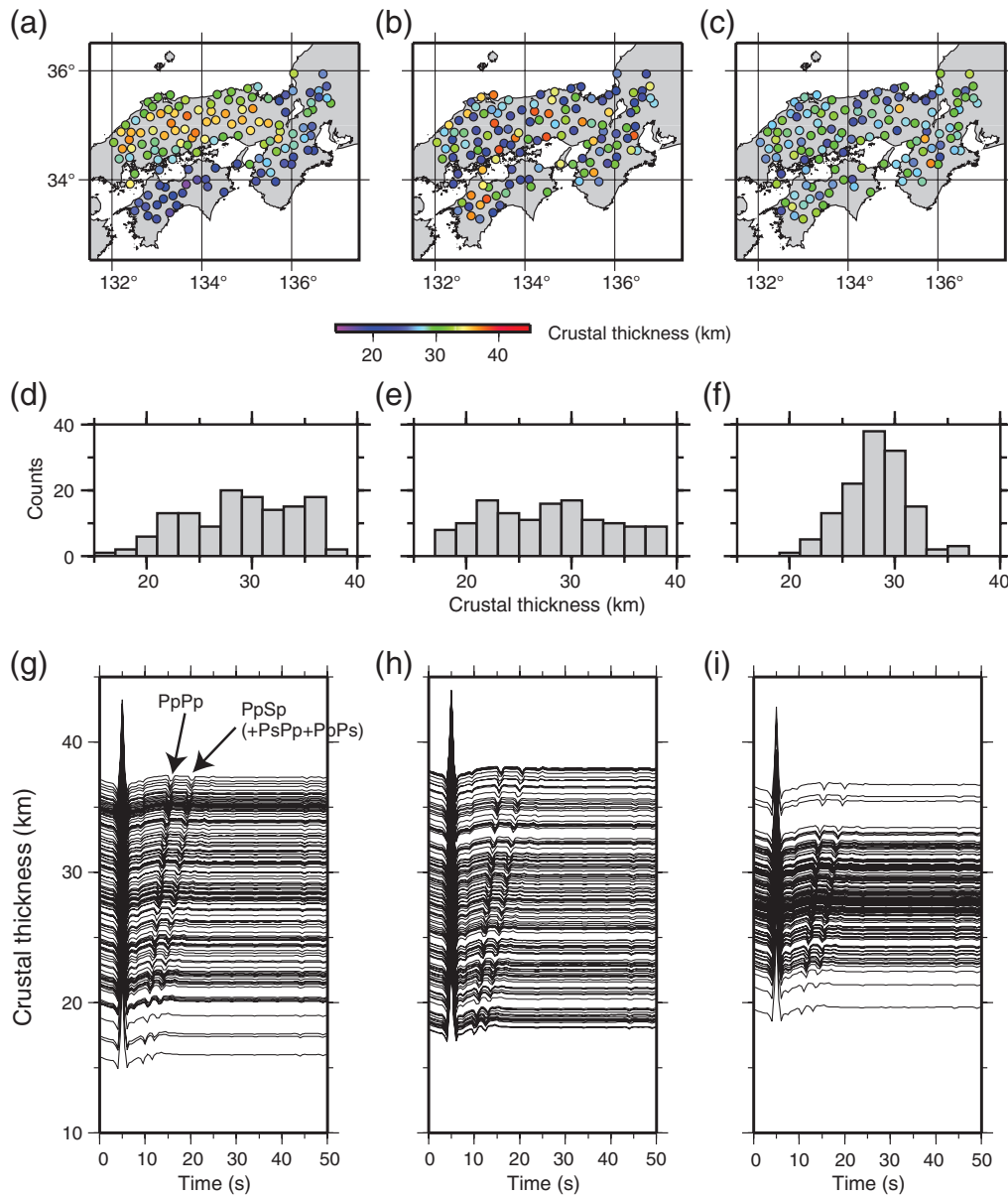
Figure 4. The distributions of crustal thickness for (a) the Observational model, (b) the Random model, and (c) the Gaussian model. (d)–(f) The histograms of crustal thickness for the three models. (g)–(i) The synthetic waveforms with a frequency band of 0.07–0.7 Hz for the three models.

source wavelet for the Gaussian model shows small negative amplitude within the time window of 12–14 s. This shows that, if the undulation of the Moho over the array is small, the later phases cannot be completely suppressed.

For comparison, Figure 5 also shows waveforms estimated by linear stacking and SVD (Freire and Ulrych, 1988) of the synthetic waveforms shown in Figure 4. For the application of SVD, we only preserved first principal component to retrieve source wavelet. Although the later arrivals reflected from the Moho seem to be suppressed for all three cases, an offset in amplitude in both the stacked waveform and waveform produced by the SVD with respect to the

original synthetic waveform can be seen in the time window of 10–20 s (Fig. 5), possibly because of the negative amplitude of the later arrivals. It appears that the source wavelet estimated by SVD tends to be similar to that from linear stacking for the three cases. However, such an offset cannot be seen in the source wavelet estimated by SA. This would therefore be an advantage of employing SA for estimating the source wavelet. Moreover, in the cases for which the seismograms employed contain noisy data, and the number of stations available over the array is small, SA would more effectively extract the source wavelet than the linear stacking technique.
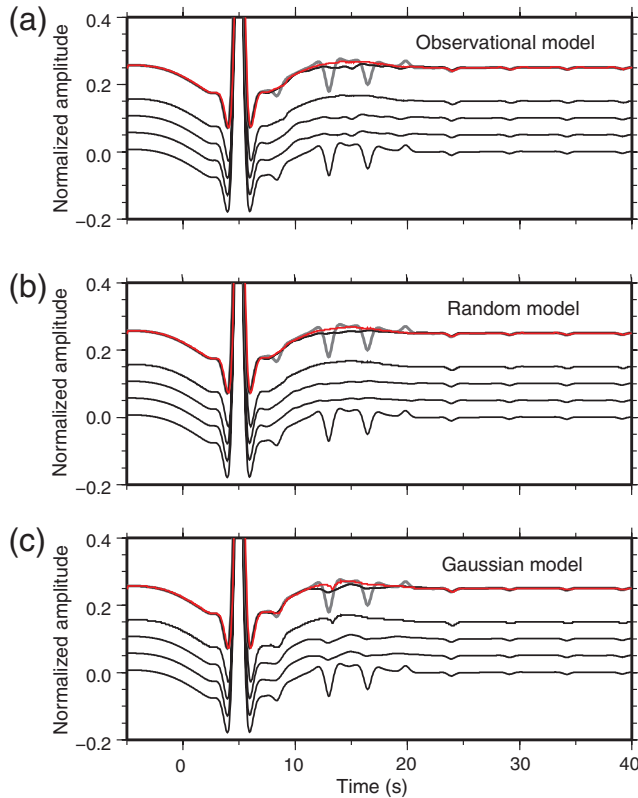
Figure 5. (a) The four overlapped waveforms at the top indicates a (gray) synthetic waveform for a crustal thickness of 28 km and the (black) source wavelets estimated from the linear stacking technique, (black) SVD, and (red) SA for the Observational model. Each trace for SA, SVD, linear stacking, and the synthetic waveform is also displayed below from second top to bottom. (b) and (c) are the same as (a), but for the Random and Gaussian models, respectively.

The vertical RFs deconvolved by the source wavelets estimated by SA for the three models are also displayed in Figure 6. In each model, the amplitudes corresponding to $PpPp$ and $PpSp$ are isolated by deconvolution. Although a small negative amplitude was retained at ~13 s in the source wavelet estimated for the Gaussian model (Fig. 5c), this appears to have a small effect on the deconvolution process.

Seismic Images Using the Three Phases

Imaging seismic structure using RFs is an effective way to confirm whether the converted/reflected phases can be successfully detected in each RF trace. The three RF traces, including two radial RFs with 0.1–0.5 Hz and 0.2–1.0 Hz frequency bands respectively for Ps and $PpPs$, and one vertical RF with a 0.1–0.5 Hz frequency band for $PpPp$, were migrated from the time to the depth domain using the 1D Japan Meteorological Agency (JMA) velocity model. It was assumed that the later phases in each of the three RF traces were due to conversion/reflection phases, that is,

$Ps/PpPs/PpPp$. The conversion/reflection points for each phase within ± 20 km width from line AA′ are projected onto each transect with a grid of 1 km (distance) $\times$ 1 km (depth) (Fig. 2).

Figure 7 shows RF images obtained using the 1D JMA velocity model for Ps (Fig. 7a), $PpPs$ (Fig. 7b), and $PpPp$ (Fig. 7c) along line AA′ (see Fig. 2). Red colors in Figure 7a,b represents positive RF amplitudes (i.e., downward velocity increase), whereas blue colors represent negative RF amplitudes (downward velocity decrease). Although the red colors in Figure 7c correspond to negative RF amplitude of $PpPp$, they represent increases in downward velocity. Figure 7d shows the summation of the images in Figure 7a–c with weightings of 0.25 for Ps, 0.3 for $PpPs$, and −0.45 for $PpPp$, with these weightings used for display purposes only.

Figure 7f shows our interpretation of the image in Figure 7d. In addition to the stacked image shown in Figure 7d, each seismic image corresponding to Ps, $PpPs$, and $PpPp$ (Fig. 7a–c, respectively) clearly shows the continental Moho. This result shows that the retrieval of $PpPp$ in vertical RFs is successfully performed using source wavelets estimated by SA.

Application of Vertical RFs to Grid-Search Techniques

After the study by Zhu and Kanamori (2000) on the grid-search technique using RFs, several studies modified the technique to estimate crustal seismic velocity and thickness. Audet *et al.* (2009) took into account the dip effect of seismic discontinuities on the resulting crustal properties in the grid-search technique. The methods proposed by Kumar and Bostock (2008) and Bostock and Kumar (2010) are useful for determining crustal V_P and V_P/V_S, which require RFs with a wide range of slowness observed at a station. For these techniques, it is important to precisely estimate travel times of the phases used with respect to the direct P wave. Although the accuracy of the pick estimation strongly depends on SNR of RFs, in the case that good quality RFs are observed at a station, crustal properties including V_P, V_P/V_S, and thickness can be obtained with no assumptions. Helffrich and Thompson (2010) employed another approach to estimate crustal V_P/V_S without determining the travel times of the phases, in which the resulting V_P/V_S does not strongly depend on V_P. In this study, we attempt to use the $PpPp$ and $PpSp$ phases that emerge in vertical RFs in the method proposed by Helffrich and Thompson (2010) to estimate crustal properties.

Advantage of the Stacking Technique Using $PpPp$ in Vertical RFs

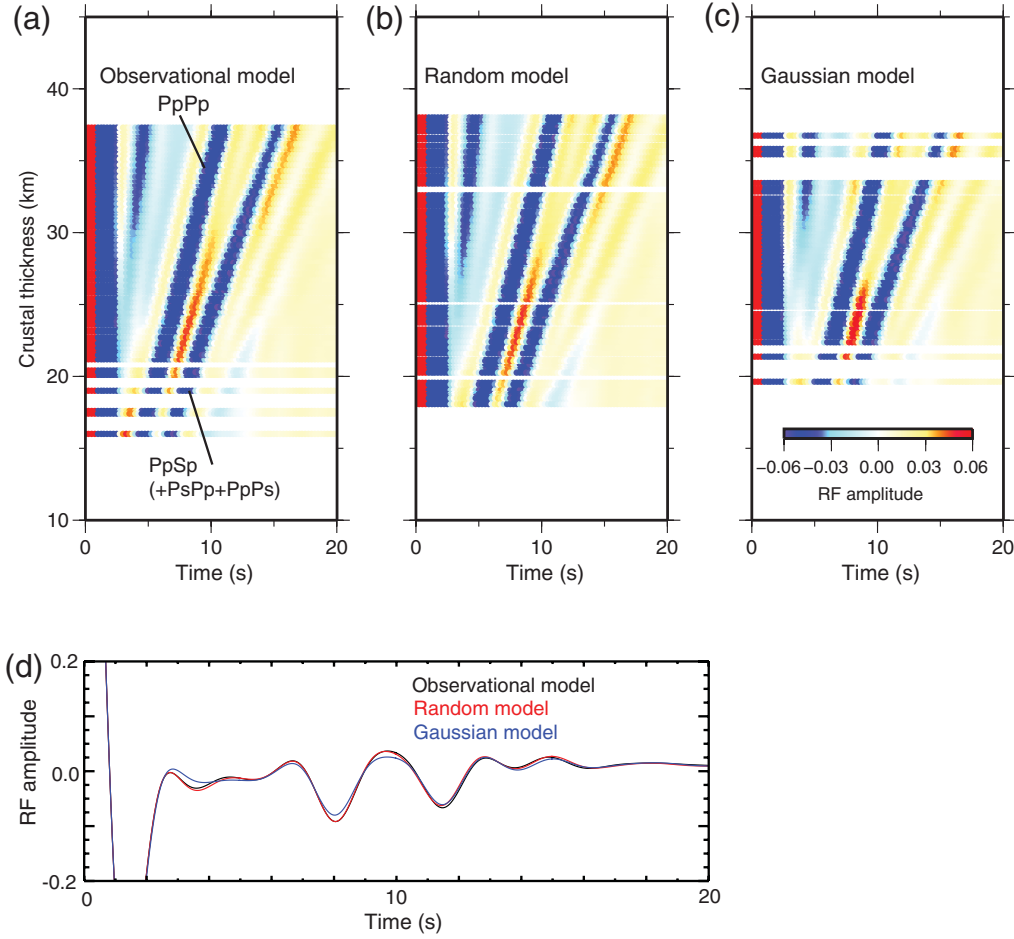Following the study of Helffrich and Thompson (2010), a quantity, X, is defined by

Figure 6. (a) The vertical RFs deconvolved by the source wavelets estimated by SA, with a frequency band of 0.1–0.5 Hz, for the Observational model. (b) and (c) are the same as (a), but for the Random and Gaussian models, respectively. In these figures, two negative phases corresponding to $PpPp$ and $PpSp$ ($+PsPp + PpPs$) can be seen. (d) Examples of vertical RFs for: (black line) the Observational model with a crustal thickness of 28.00 km, (red line) the Random model with a crustal thickness of 27.95 km, and (blue line) the Gaussian model with a crustal thickness of 28.00 km.

$$X = \frac{R^2 - p^2 V_P^2}{1 - p^2 V_P^2} = \frac{\eta^2}{\xi^2}, \qquad (3)$$

where $R = V_P/V_S$, p is slowness, and ξ and η are vertical slownesses of P and S waves (i.e., $\xi = \sqrt{\frac{1}{V_P^2} - p^2}$, $\eta = \sqrt{\frac{1}{V_S^2} - p^2}$). Using the quantity X, the relations of the travel times of Ps, $PpPs$, $PpSs$, $PpPp$, and $PpSp$ can be written as

$$t_{PpPs}(X) = t_{Ps}(\sqrt{X} + 1)/(\sqrt{X} - 1),$$
$$t_{PpSs}(X) = t_{Ps}2\sqrt{X}/(\sqrt{X} - 1),$$
$$t_{PpPp}(X) = t_{Ps}2/(\sqrt{X} - 1), \quad \text{and}$$
$$t_{PpSp}(X) = t_{PpPs}. \qquad (4)$$

The derivatives of the travel times with respect to slowness are also obtained as

$$\frac{dt_{Ps}}{dp} = \frac{2pt_{Ps}^2}{\xi^2(\sqrt{X} - 1)^2}\left(\frac{1}{t_{PpPs} - t_{Ps}} - \frac{1}{t_{PpPs} + t_{Ps}}\right),$$
$$\frac{dt_{PpPs}}{dp} = \frac{-2pt_{Ps}^2}{\xi^2(\sqrt{X} - 1)^2}\left(\frac{1}{t_{PpPs} - t_{Ps}} + \frac{1}{t_{PpPs} + t_{Ps}}\right),$$
$$\frac{dt_{PpSs}}{dp} = \frac{-2pt_{Ps}^2}{\xi^2(\sqrt{X} - 1)^2}\left(\frac{1}{t_{PpSs}}\right),$$
$$\frac{dt_{PpPp}}{dp} = \frac{-2pt_{Ps}^2}{\xi^2(\sqrt{X} - 1)^2}\left(\frac{1}{t_{PpPp}}\right), \quad \text{and}$$
$$\frac{dt_{PpSp}}{dp} = \frac{dt_{PpPs}}{dp}. \qquad (5)$$

For the case $t_{Ps} = 3.40$ s, $V_P = 6.35$ km/s, and the reference slowness $p = 0.065$ s/km, we can obtain relations between Ps, $PpPs$, $PpSs$, $PpPp$, and $PpSp$ in the t-X domain using equation (4), as shown in Figure 8a. The intersection of the curves represents the preferred values of X and t_{Ps}. In particular, the curve corresponding to $PpPp$ crosses that for Ps with a larger angle than those for $PpPs$, $PpSs$, and $PpSp$, which indicates that the value of X could be
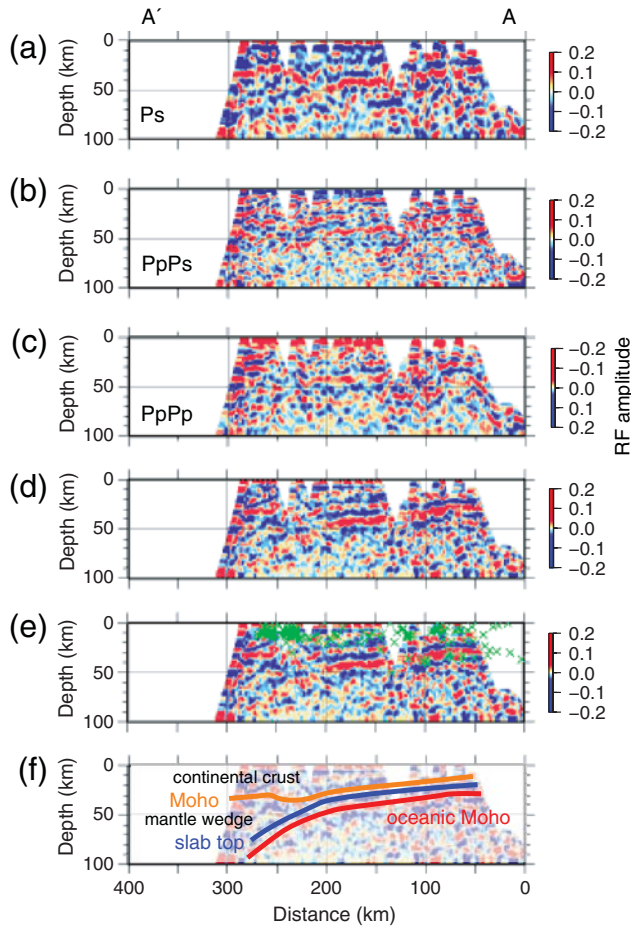
Figure 7. RF images along line AA′ using the 1D JMA velocity model. (a) Seismic image of *Ps* within a frequency band of 0.2–1.0 Hz. (b) Seismic image of *PpPs* within a frequency band of 0.1–0.5 Hz. (c) Seismic image of *PpPp* within a frequency band of 0.1–0.5 Hz. (d) Summation of (a)–(c) with weightings of 0.25 for *Ps*, 0.3 for *PpPs*, and −0.45 for *PpPp*. (e) as (d), but with the hypocenter distribution determined using the 1D JMA velocity model (green + symbols). (f) interpretation of (d). Orange, blue, and red lines represent the continental Moho, the upper surface of the slab, and the oceanic Moho, respectively. The converted and reflected points within 20 km of each line were stacked onto the cross sections (Fig. 2).

determined more precisely by taking into account the contribution of *PpPp* in the *t-X* stack. In case that the t_{Ps} is required, the contribution of *PpPp* would not be useful (Fig. 8a). However, when RFs have a low SNR, it would be better to incorporate all of the phases in the *t-X* stack. With a suite of RFs, using equations (4) and (5), the amplitudes of the five phases along the predicted travel-time curves for the observed range of slowness can be stacked in the t_{Ps}-X domain with respect to reference slowness.

Synthetic Test for Stacking Techniques Using Vertical RFs

Using the method of Langston (1977), we calculated synthetic waveforms from radial and vertical components

for a slowness range of 0.06–0.08 s/km at intervals of 0.005 s/km. We used the Observational model (Fig. 4a) for velocity structures ($V_P = 6.35$ km/s, $V_S = 3.65$ km/s, $V_P/V_S = 1.7397$) and crustal thickness, and chose a station at which the crustal thickness was 28.0 km. For the estimation of the source wavelet by SA, we used a frequency band of 0.07–0.7 Hz for synthetic waveforms on the vertical component. In the deconvolution process, we also applied bandpass filters of 0.2–1.0 Hz and 0.1–0.5 Hz for the radial RF, and 0.1–0.5 Hz for the vertical RF.

As shown in Figure 8c, the *t-X* stack that uses five phases, *Ps*, *PpPs*, *PsSs*, *PpPp*, and *PpSp*, results in $V_P/V_S = 1.739 \pm 0.075$ and a crustal thickness of 27.73 ± 2.74 km, which is in good agreement with the initial values of V_P/V_S and the thickness. The 1σ uncertainty was estimated using the method of Zhu and Kanamori (2000), using the stacked amplitude of the five phases with appropriate weightings ($Ps = 1$, $PpPs = 1$, $PsSs = -1$, $PpPp = -1$, and $PpSp = -1$) for each source–receiver pair. Errors in stacking techniques could be caused by (1) wave-duration dependence on the frequency component of RFs, (2) the variations in the conversion/reflection coefficients of the seismic phases, (3) SNR of the RFs employed, and (4) relations between the phases used in the stacking domain, such as the one shown in Figure 8a. In particular for (2), the conversion/reflection coefficients of phases vary as a function of slowness, which could potentially produce significant errors in stacking techniques. Figure 8b shows the conversion/reflection coefficients of the five phases and the stacked amplitudes of the five phases with the above weightings. The coefficients of *PpPs* and *PsSs* are comparable over the slowness range. The relatively large absolute coefficients of *Ps* and *PpPp* vary linearly as a function of slowness. The summation of the two phases with the above weightings produces comparable amplitudes over the slowness range. Based on these observations, it seems that the error is expected to be small in the *t-X* stack using all phases except for *PpSp*. As a result, the *t-X* stack using four phases results in $V_P/V_S = 1.739 \pm 0.034$ and a crustal thickness of 27.73 ± 1.26 km (Fig. 8d). Although the errors showed an improvement on the previous case, it would be useful to determine which phases should be employed in the stacking by taking into account the SNR of RFs.

We also used the phases on the vertical RF in the method of Zhu and Kanamori (2000). Figure 8e shows relations of the five phases as a function of V_P/V_S and crustal thickness, with the same parameters of crustal structure as those in the previous *t-X* stack. The resulting values of V_P/V_S and crustal thickness are estimated to be 1.736 ± 0.027 and 27.90 ± 1.20 km (Fig. 8f). Although the errors are smaller than those obtained in the *t-X* stack, the contributions of *PpPp* and *PpSp* would be useful for determining the two parameters, as described above for the *t-X* stack.
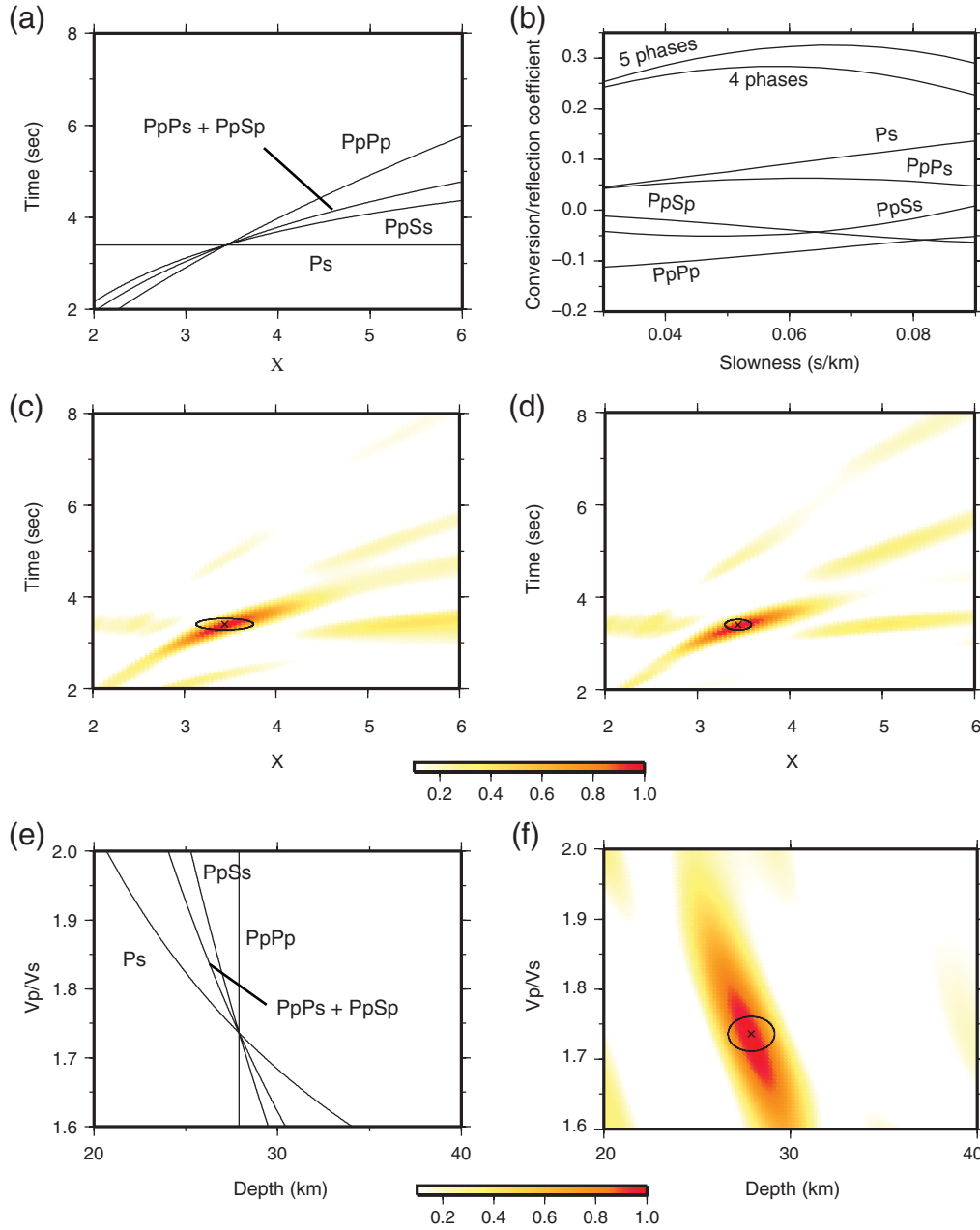
Figure 8. Synthetic test using vertical RFs in the grid-search technique. (a) Dependence of travel times of Ps, $PpPs$, $PpSs$, $PpPp$, and $PpSp$ with respect to the direct P wave as a function of X in equation (4). (b) Conversion/reflection coefficients of the five phases. The values of $V_P = 6.35$ km/s and $V_S = 3.65$ km/s at the crust, and the mantle-velocity structure of the IASP91 velocity model (Kennett and Engdahl, 1991) are used. The densities of the crust and mantle are assumed to be 2.70 g/cm^3 and 3.38 g/cm^3. The labels, 5 phases and 4 phases, indicate the summed amplitudes from all five phases and from four phases excluding $PpSp$, with weights of $Ps = 1$, $PpPs = 1$, $PpSs = -1$, $PpPp = -1$, and $PpSp = -1$. (c) Result for grid search using the five phases. The ellipse indicates the 1σ uncertainty. (d) is the same as (c), but for only four phases, excluding $PpSp$. (e) is the same as (a), but for the method of Zhu and Kanamori (2000). (f) is the same as (c), but for the stacking result using the method of Zhu and Kanamori (2000).

Application of a Grid Search to the Observed RFs

We applied the t-X stack using radial and vertical RFs to records from two Hi-net stations in southwestern Japan, SSKH and KACH (Fig. 2; Fig. 9). The values of V_P are chosen to be 6.0 km/s for SSKH and 6.35 km/s for KACH. The lower value of V_P at SSKH reflects the presence of an accretionary prism (Ito *et al.*, 2009). Because Figure 9d,h displays relatively large amplitudes of $PpSp$ within the slowness range of 0.07–0.08 s/km, for which the number of RFs is largest, we used five phases in the t-X stack. The resulting V_P/V_S and crustal thickness were estimated to be 1.705 ± 0.087 and 17.86 ± 2.16 km for SSKH (Fig. 9a–d), and
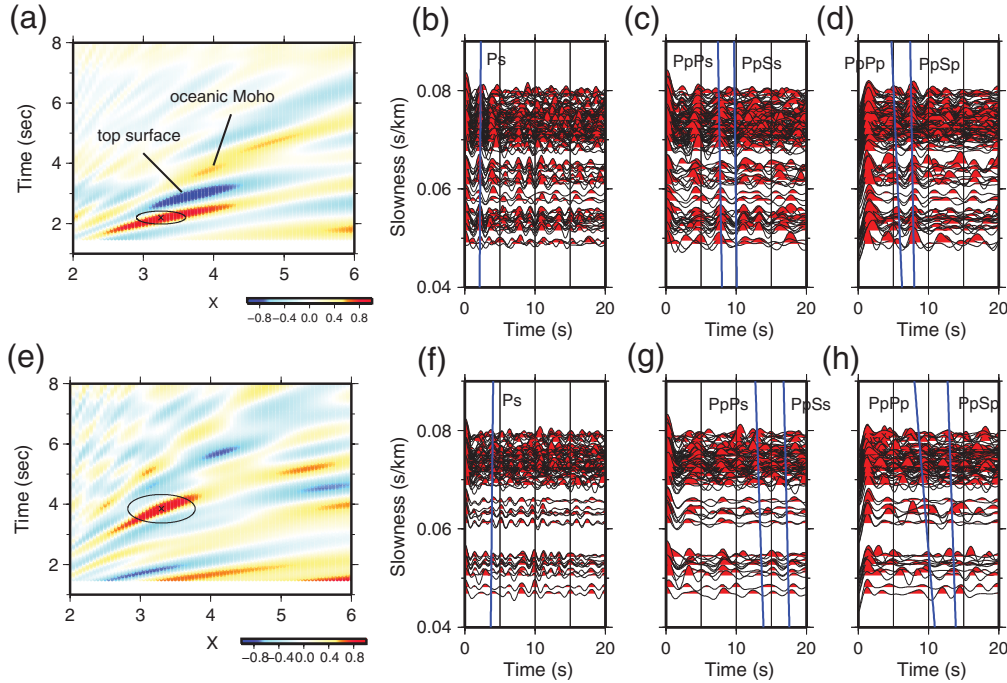
Figure 9. Results of the grid search using the observed RFs. (a) RF stacking for t_{ps} and X for station SSKH. The ellipse indicates 1σ uncertainty. (b) Radial RFs for 0.2–1.0 Hz used in the stacking. (c)–(d) As (b), but for radial RFs for 0.1–0.5 Hz, and vertical RFs for 0.1–0.5 Hz. Blue lines represent travel times of Ps, $PpPs$, $PpSs$, $PpPp$, and $PpSp$ as a function of slowness, as predicted by the values of t_{Ps}, X, and equation (5). (e)–(h) are the same as (a–d), but for station KACH.

1.705 ± 0.117 and 32.87 ± 5.31 km for KACH (Fig. 9e–h). Figure 9a also shows negative and positive peaks at lag times of 3 and 3.8 s and at an X range of 3.5–4, which correspond to the top surface and oceanic Moho of the Philippine Sea slab. In addition, we evaluated how the variation in V_P influences the resulting V_P/V_S and crustal thickness. The results for a V_P range of 5.5–7.0 km/s are shown in Figure 10. The gray-shaded regions represent areas within a range of $\pm 5\%$ of the value of V_P above selected and within $1/2\sigma$ of the resulting V_P/V_S and crustal thickness. The crustal thickness results for the two stations show relatively large variations with respect to the variation in V_P, whereas the estimation of V_P/V_S is quite stable over the V_P range. In addition to the contribution of $PpPp$ in constraining the value of X, this stability would also be useful for precisely determining V_P/V_S within the crust. In cases when the accurate estimation of crustal thickness is required, it would be better if the value of V_P were determined by referring to tomographic velocity models or exploration surveys.

Seismic Imaging for Enhancing Horizontal Discontinuities

Here, we propose a technique that enhances subsurface horizontal discontinuities in seismic images, through t_{Ps}-p stacking using equations (4) and (5), and the amplitudes of the five phases. Given a reference slowness, p^0, of a teleseismic P wave, t_{Ps} as a function of depth, $t_{Ps}(p^0, H)$, can be calculated by assuming a 1D velocity profile, for which H

is depth. Alternatively, depth as a function of t_{Ps}, $H(p^0, t_{Ps})$, with a constant t_{Ps} interval can be estimated by interpolating $t_{Ps}(p^0, H)$. Averaging V_P and V_S in the velocity model between the ground surface and $H(p^0, t_{Ps})$, the quantity X, as a function of H, can also be determined with equation (3). We can now obtain the values of $H(p^0, t_{Ps})$, $X(p^0, t_{Ps})$, and the averaged $V_P(p^0, t_{Ps})$ and $V_S(p^0, t_{Ps})$. Using equations (4) and (5), the arrival times of the five phases on all RF traces, which have a slowness p, can be predicted with respect to a pair of the variables (p^0, t_{Ps}), thus the amplitudes of the five phases for the employed traces can be stacked with respect to (p^0, t_{Ps}), and then at other points within a range of t_{Ps}. Finally, the same process is performed again, changing the reference slowness within a slowness range.

We assume the 1D JMA velocity model, and perform a t_{Ps}-p stack using the five phases on radial and vertical RFs observed at a station over t_{Ps} ranges of 0.05–15 s and p ranges of 0.03–0.09 s/km. The weights are the same as those used in the Synthetic Test for Stacking Techniques Using Vertical RFs section. As an example, Figure 11a,b represents t_{Ps}-p stacks for SSKH and KACH. Arrows at 2 s (Fig. 11a) and at 4 s (Fig. 11b) indicate positive signals corresponding to the Moho. These lag times of Ps are in good agreement with the results in Figure 9a and e. In addition, if the slowness and back-azimuth information of each RF observed at a station are retained, traces corresponding to the source–receiver pairs of the RFs can be retrieved from the t_{Ps}-p stack result, and can be migrated to depth-domain RFs using the
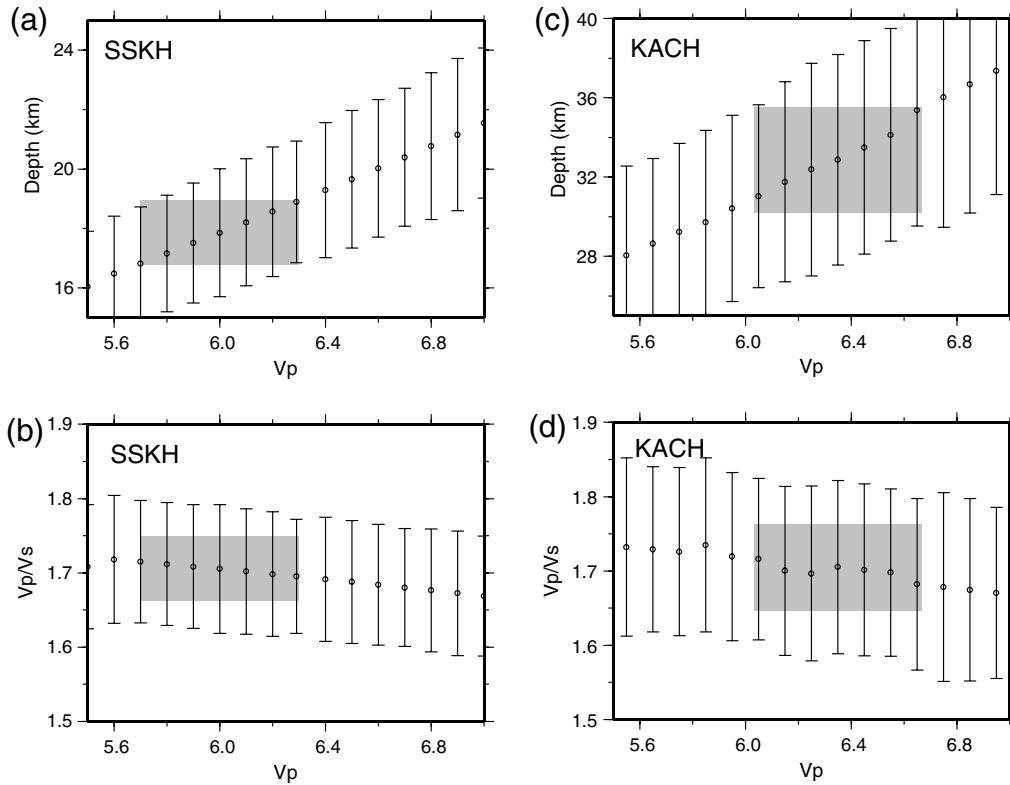
Figure 10. Variations in crustal thickness and V_P/V_S as a function of the initial value of V_P. (a) Relation between crustal thickness and the initial value of V_P for station SSKH. (b) Relation between V_P/V_S and the initial value of V_P for station SSKH. (c)–(d) are the same as (a–b), but for station KACH. The gray-shaded regions indicate areas within a range of $\pm 5\%$ from the initial value of V_P and $1/2\sigma$ from the resulting V_P/V_S and crustal thickness provided by the grid search.
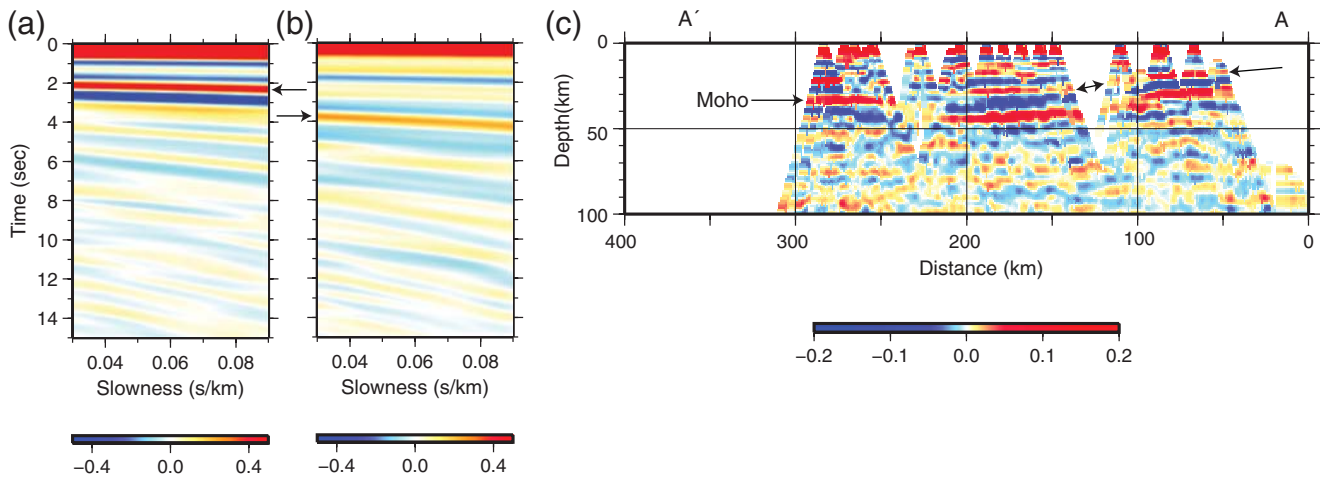

Figure 11. Results of t_{Ps}–p stack and seismic image. (a) Result of t_{Ps}–p stack for station SSKH, estimated using the five phases; (b) is the same as (a), but for station KACH; (c) seismic image along AA′ using the five phases, with enhanced horizontal discontinuities. The label and solid lines indicate signals corresponding to the Moho.

1D JMA velocity model. Figure 11c shows a seismic image along AA′ using the five phases. Because equation (5) shows the gradient of travel time with respect to slowness for a horizontal discontinuity, signals generated from dipping discontinuities cannot be stacked coherently using equation (5). Therefore, in the seismic image, horizontal or weakly dip-

ping discontinuities are enhanced in Figure 11c. In particular, signals for the Moho can be more easily traced in the northern part of AA′, compared with Figure 7d. Referring to such seismic images that enhance the signals from horizontal boundaries, we would be able to select stations at which the grid-search techniques can be applied. In particular, the

information may be useful for estimating the averaged V_P/V_S and thicknesses from the ground surface to the top slab surface and oceanic Moho, because these boundaries can be regarded as a horizontal discontinuity at some regions in southwestern Japan (Fig. 11c).

Discussion and Conclusion

We determined crustal properties of V_P/V_S and crustal thickness from five seismic phases (Ps, $PpPs$, $PpSs$, $PpPp$, and $PpSp$) extracted from radial and vertical RFs. Using a nonlinear waveform analysis (SA), the source wavelet of the teleseismic P wave can be estimated using records from the vertical components of an array of seismometers. The vertical RF is calculated by deconvolution of the vertical component by the source wavelet. To successfully estimate the source wavelet of the teleseismic P wave, the following conditions are desirable: (1) the source wavelet of the teleseismic P wave is the same throughout the array, and there exist large lateral variations in the depth of seismic discontinuities beneath the stations within the array; and (2) the direct P wave has a larger amplitude than that of later arrivals in the record. Although whether $PpPp$ generated at the Moho can be removed from the source wavelet using SA strongly depends on the degree of undulation of the Moho underneath the array, we demonstrated with numerical simulations that a good source wavelet could be obtained for the configuration of the Moho in southwestern Japan. Each RF image (i.e., those obtained using Ps, $PpPs$, and $PpPp$) and the stacked image are successful in showing the continental Moho, the oceanic Moho, and the upper surface of the Philippine Sea slab beneath southwestern Japan. This confirms that $PpPp$ can be detected by the approach used in this study. Moreover, using the $PpPp$ obtained in a grid-search technique is useful for determining crustal thickness, and V_P/V_S. The use of $PpSp$ in vertical RFs can also contribute to increasing SNR ratio of the stacked image.

Data and Resources

Hi-net data is available at http://www.hinet.bosai.go.jp/ (last accessed December 2012), which is operated by National Research Institute for Earth Science and Disaster Prevention (NIED). The Japan Meteorological Agency (JMA) catalog data is open to the public (http://www.hinet.bosai.go.jp/REGS/JMA/list/; last accessed December 2012), also maintained by the NIED. Some plots were made by using the Generic Mapping Tools (GMT; Wessel and Smith, 1991).

Acknowledgments

References

Ammon, C. J. (1991). The isolation of receiver effects from teleseismic *P* waveforms, *Bull. Seismol. Soc. Am.* **81,** 2504–2510.

Audet, P., M. G. Bostock, N. I. Christensen, and S. M. Peacock (2009). Seismic evidence for overpressured subducted oceanic crust and megathrust fault sealing, *Nature* **457,** 76–78, doi: 10.1038/nature07650.

Bostock, M. G. (1999). Seismic waves converted from velocity gradient anomalies in the Earth's upper mantle, *Geophys. J. Int.* **138,** 747–756.

Bostock, M. G., and M. R. Kumar (2010). Bias in seismic estimates of crustal properties, *Geophys. J. Int.* **182,** 403–407.

Bostock, M. G., and S. Rondenay (1999). Migration of scattered teleseismic body waves, *Geophys. J. Int.* **137,** 732–746.

Bostock, M. G., S. Rondenay, and J. Shragge (2001). Multiparameter two-dimensional inversion of scattered teleseismic body waves 1. Theory for oblique incidence, *J. Geophys. Res.* **106,** no. B12, 30,771–30,782.

Box, G. E. P., and M. E. Muller (1958). A note on the generation of random normal deviates, *Ann. Math. Stat.* **29,** no. 2, 610–611, doi: 10.1214/aoms/1177706645.

Chevrot, S. (2002). Optimal waveform and delay time analysis by simulated annealing, *Geophys. J. Int.* **151,** 164–171.

Chevrot, S., and D. van der Hilst (2000). The poisson ratio of the Australian crust: Geological and geophysical implications, *Earth Planet. Sci. Lett.* **183,** 121–132.

Ferris, A., G. A. Abers, D. H. Christensen, and E. Veenstra (2003). High resolution image of the subducted Pacific plate beneath central Alaska, 50–150 km depth, *Earth Planet. Sci. Lett.* **214,** 575–588.

Freire, S. L. M., and T. J. Ulrych (1988). Application of singular value decomposition to vertical seismic profiling, *Geophysics* **53,** 778–785.

Garcia, R., S. Chevrot, and M. Weber (2004). Nonlinear waveform and delay time analysis of triplicated core phases, *J. Geophys. Res.* **109,** no. B1, doi: 10.1029/2003JB002429.

Hayashida, T., F. Tajima, and J. Mori (2010). Improved seismic velocity structure in southwestern Japan using pronounced *sP* phases recorded for intraslab earthquakes, *Bull. Seismol. Soc. Am.* **100,** 1928–1939.

Helffrich, G., and D. Thompson (2010). A stacking approach to estimate Vp/Vs from receiver functions, *Geophys. J. Int.* **182,** 899–902.

Hirose, F., J. Nakajima, and A. Hasegawa (2008). Three-dimensional seismic velocity structure and configuration of the Philippine Sea slab in southwestern Japan estimated by double-difference tomography, *J. Geophys. Res.* **113,** B09315, doi: 10.1029/2007JB005274.

Ide, S., K. Shiomi, K. Mochizuki, T. Tonegawa, and G. Kimura (2010). Split Philippine Sea plate beneath Japan, *Geophys. Res. Lett.* **37,** L21304, doi: 10.1029/2010GL044585.

Iritani, R., N. Takeuchi, and H. Kawakatsu (2010). Seismic attenuation structure of the top half of the inner core beneath the northeastern Pacific, *Geophys. Res. Lett.* **37,** L19303, doi: 10.1029/2010GL044053.

Ito, T., Y. Kojima, S. Kodaira, H. Sato, Y. Kaneda, T. Iwasaki, E. Kurashimo, N. Tsumura, A. Fujiwara, T. Miyauchi, N. Hirata, S. Harder, K. Miller, A. Murata, S. Yamakita, M. Onishi, S. Abe, T. Sato, and T. Ikawa (2009). Crustal structure of southwest Japan, revealed by the integrated seismic experiment Southwest Japan 2002, *Tectonophysics* **472,** 124–134.

Katsumata, A. (2010). Depth of the Moho discontinuity beneath the Japanese Islands estimated by traveltime analysis, *J. Geophys. Res.* **115,** B04303, doi: 10.1029/2008JB005864.

Kawakatsu, H., and S. Watada (2007). Seismic evidence for deep-water transportation in the mantle, *Science* **316,** 1468–1471.

Kawakatsu, H., and S. Yoshioka (2011). Metastable olivine wedge and deep dry cold slab beneath southwest Japan, *Earth Planet. Sci. Lett.* **303,** 1–10.

Kennett, B. L. N., and E. R. Engdahl (1991). Travel times for global earthquake location and phase identification, *Geophys. J. Int.* **105,** 429–465.

Kind, R., G. L. Kosarev, and N. V. Petersen (1995). Receiver functions of the stations of the German Regional Seismic Network (GRSN), *Geophys. J. Int.* **121,** 191–202.

Kumar, M. R., and M. G. Bostock (2008). Extraction of absolute P velocity from receiver functions, *Geophys. J. Int.* **175,** 515–519.

Langston, C. A. (1977). The effect of planar dipping structure on source and receiver responses for constant ray parameter, *Bull. Seismol. Soc. Am.* **67,** no. 4, 1029–1050.

Langston, C. A. (1979). Structure under Mount Rainier, Washington, inferred from teleseismic body waves, *J. Geophys. Res.* **84,** 4749–4762.

Langston, C. A., and J. K. Hammer (2001). The vertical component *P*-wave receiver function, *Bull. Seismol. Soc. Am.* **91,** 1805–1819.

Li, X.-Q., and J. L. Nábělek (1999). Deconvolution of teleseismic body waves for enhancing structure beneath a seismometer array, *Bull. Seismol. Soc. Am.* **89,** 190–201.

Li, X., S. V. Sobolev, R. Kind, X. Yuan, and Ch. Estabrook (2000). A detailed receiver function image of the upper mantle discontinuities in the Japan subduction zone, *Earth Planet. Sci. Lett.* **183,** 527–541.

Matsubara, M., K. Obara, and K. Kasahara (2008). Three-dimensional *P*- and *S*-wave velocity structures beneath the Japan islands obtained by high-density seismic stations by seismic tomography, *Tectonophysics* **454,** 86–103.

Miyazaki, S., and K. Heki (2001). Crustal velocity field of southwest Japan: Subduction and arc-arc collision, *J. Geophys. Res.* **106,** 4305–4326.

Miyoshi, T., and K. Ishibashi (2004). Geometry of the seismic Philippine Sea slab beneath the region from Ise Bay to western Shikoku, southwest Japan, *Zisin* **57,** 139–152 (in Japanese with English abstract).

Nakajima, J., and A. Hasegawa (2007). Subduction of the Philippine Sea plate beneath southwestern Japan: Slab geometry and its relationship to arc magmatism, *J. Geophys. Res.* **112,** B08306, doi: 10.1029/2006JB004770.

Nishida, K., H. Kawakatsu, and K. Obara (2008). Three-dimensional crustal S wave velocity structure in Japan using microseismic data recorded by Hi-net tiltmeters, *J. Geophys. Res.* **113,** B10302, doi: 10.1029/2007JB005395.

Okada, Y., K. Kasahara, S. Hori, K. Obara, S. Sekiguchi, H. Fujiwara, and A. Yamamoto (2004). Recent progress of seismic observation networks in Japan -Hi-net, F-net, K-NET and KiK-net-, *Earth Planets Space* **56,** xv–xxviii.

Owens, T., G. Zandt, and S. R. Taylor (1984). Seismic evidence for an ancient rift beneath the Cumberland Plateau, Tennessee: A detailed analysis of broadband teleseismic *P* waveforms, *J. Geophys. Res.* **89,** 7783–7795.

Ramesh, D. S., H. Kawakatsu, S. Watada, and X. Yuan (2005). Receiver function images of the central Chugoku region in the Japanese islands using Hi-net data, *Earth Planets Space* **57,** 271–280.

Reading, A., B. L. N. Kennett, and M. Sambridge (2003). Improved inversion for seismic structure using transformed, *S*-wave vector receiver functions: Removing the effect of the free surface, *Geophys. Res. Lett.* **30,** 1981, doi: 10.1029/2003GL018090.

Rondenay, S., M. G. Bostock, and J. Shragge (2001). Multiparameter two-dimensional inversion of scattered teleseismic body waves, 2. Application to the Cascadia 1993 data set, *J. Geophys. Res.* **106,** no. B12, 30,795–30,807.

Sen, M., and P. Stoffa (1995). *Global Optimization Methods in Geophysical Inversion*, Elsevier Sci., New York, 281 pp.

Sheehan, A. F., G. A. Abers, C. H. Jones, and A. L. Lerner-Lam (1995). Crustal thickness variations across the Colorado Rocky Mountains from teleseismic receiver functions, *J. Geophys. Res.* **100,** 20,391–20,414.

Shiomi, K., K. Obara, and H. Sato (2006). Moho depth variation beneath southwestern Japan revealed from the velocity structure based on receiver function inversion, *Tectonophysics* **420,** 205–221.

Shiomi, K., H. Sato, K. Obara, and M. Ohtake (2004). Configuration of subducting Philippine Sea plate beneath southwest Japan revealed from receiver function analysis based on the multivariate autoregressive model, *J. Geophys. Res.* **109,** B04308, doi: 10.1029/2003JB002774.

Shragge, J., M. G. Bostock, and S. Rondenay (2001). Multiparameter two-dimensional inversion of scattered teleseismic body waves 2. Numerical examples, *J. Geophys. Res.* **106,** no. B12, 30,783–30,793.

Ueno, T., T. Shibutani, and K. Ito (2008a). Configuration of the continental Moho and Philippine Sea slab in southwest Japan derived from receiver function analysis: Relation to subcrustal earthquakes, *Bull. Seismol. Soc. Am.* **98,** no. 5, 2416–2427, doi: 10.1785/0120080016.

Ueno, T., T. Shibutani, and K. Ito (2008b). Subsurface structures derived from receiver function analysis and relation to hypocenter distributions in the region from the eastern Shikoku to the northern Chugoku districts, Southwest Japan, *Earth Planets Space* **60,** 573–579.

Wessel, P., and W. H. F. Smith (1991). Free software helps map and display data, *Eos Trans. AGU* **72,** no. 41, 441, doi: 10.1029/90EO00319.

Wilson, D., and R. Aster (2005). Seismic imaging of the crust and upper mantle using regularized joint receiver functions, frequency–wave-number filtering, and multimode Kirchhoff migration, *J. Geophys. Res.* **110,** B05305, doi: 10.1029/2004JB003430.

Yamauchi, M., K. Hirahara, and T. Shibutani (2003). High resolution receiver function imaging of the seismic velocity discontinuities in the crust and the uppermost mantle beneath southwest Japan, *Earth Planets Space* **55,** 59–64.

Yuan, X., S. V. Sobolev, R. Kind, O. Oncken, G. Bock, G. Asch, B. Schurr, F. Graeber, A. Rudloff, W. Hanka, K. Wylegalla, R. Tibi, C. Haberland, A. Rietbrock, P. Giese, P. Wigger, P. Rower, G. Zandt, S. Beck, T. Wallace, M. Pardo, and D. Comte (2000). Subduction and collision processes in the Central Andes constrained by converted seismic phases, *Nature* **408,** 958–961.

Zandt, G., S. C. Myers, and T. C. Wallace (1995). Crust and mantle structure across the basin and range Colorado Plateau boundary at 37-degree-N latitude and implications for Cenozoic extensional mechanism, *J. Geophys. Res.* **100,** 10,529–10,548.

Zhu, L. P., and H. Kanamori (2000). Moho depth variation in southern California from teleseismic receiver functions, *J. Geophys. Res.* **105,** 2969–2980.

Institute for Research on Earth Evolution
Japan Agency for Marine-Earth Science and Technology
3173-25, Syowa-machi, Kanazawa-ku
Yokohama 236-0001, Japan
tonegawa@jamstec.go.jp
    (T.T.)

Earthquake Research Institute
The University of Tokyo
1-1-1 Yayoi, Bunkyo-ku
Tokyo 113-0032
    (R.I., H.K.)